photonics

MDPI

Article

High-Performance Vis–NIR Photodetectors Based on Two-Dimensional Bi_2Te_3 Thin Film and Applications

Zhendong Fu [1], Xuefang Liu [2], Fuguo Wang [2,3], Langlang Du [2], Wenbao Sun [1,*], Yueyu Sun [1], Xiaoxian Song [2,3,*], Haiting Zhang [2] and Jianquan Yao [2,3]

[1] Center of Intelligent Opto-Electric Sensors, Tianjin Jinhang Technical Physics Institute, Tianjin 300308, China; fzd199@126.com (Z.F.); syy100@163.com (Y.S.)
[2] School of Mechanical Engineering, Jiangsu University, Zhenjiang 212013, China; 2232103008@stmail.ujs.edu.cn (X.L.); 2222003032@stmail.ujs.edu.cn (F.W.); 2222203040@stmail.ujs.edu.cn (L.D.); zhanghaiting@ujs.edu.cn (H.Z.); jqyao@tju.edu.cn (J.Y.)
[3] School of Precision Instrument and Opto-Electronics Engineering, Tianjin University, Tianjin 300072, China
* Correspondence: sunwenbao@tju.edu.cn (W.S.); songxiaoxian@ujs.edu.cn (X.S.)

Abstract: Two-dimensional materials have excellent optoelectronic properties and have great significance in the field of photodetectors. We have prepared a thin film photodetector based on bismuth telluride (Bi_2Te_3) topological insulator using dual-temperature-zone vapor deposition technology. Due to the high-quality lattice structure of Bi_2Te_3 and the uniform and dense surface morphology of the Bi_2Te_3 thin film, the device exhibits excellent photoelectric response and Vis–NIR spectral range. Under 405 nm illumination, the responsivity is 5.6 mA/W, the specific detectivity is 1.22×10^7 Jones, and the response time is 262/328 ms. We designed a photodetector single-point scanning imaging system and successfully achieved high-resolution imaging at a wavelength of 532 nm. This work provides guidance for the application of two-dimensional materials, especially Bi_2Te_3, in the fields of photodetectors and imaging.

Keywords: Bi_2Te_3; semiconductors; photodetector; topological insulator; two-dimensional

Citation: Fu, Z.; Liu, X.; Wang, F.; Du, L.; Sun, W.; Sun, Y.; Song, X.; Zhang, H.; Yao, J. High-Performance Vis–NIR Photodetectors Based on Two-Dimensional Bi_2Te_3 Thin Film and Applications. *Photonics* **2024**, *11*, 1052. https://doi.org/10.3390/photonics11111052

Received: 10 October 2024
Revised: 6 November 2024
Accepted: 7 November 2024
Published: 9 November 2024

1. Introduction

Photodetectors (PDs) can convert light signals into electrical signals and have broad application prospects in sensing [1], measurement [2], imaging [3], artificial nociceptors [4], health monitoring [5] and communication fields [6]. Materials such as perovskite [7], quantum dot [8] and graphene [9] are considered the future of PDs. Two-dimensional (2D) materials have become promising candidates for optoelectronic devices due to their ultra-thin thickness, tunable bandgap, free dangling bonds and mechanical flexibility [10]. 2D materials do not have lattice mismatches because they are covalently bonded in-plane and out-of-plane bonded by weak van der Waals forces [11]. One such 2D material is Bi_2Te_3, a V-VI semiconductor compound with a rhombic crystal structure, belonging to the R-3m space group [12]. The Bi-Te in the crystal plane within the layer is bound by covalent and ionic bonds [13]. At the same time, Bi_2Te_3 is a topological insulator with an insulating body state and conductive surface state [14], and its electrons and holes can be quickly transferred through the surface state [15]. All of the above characteristics make Bi_2Te_3 an ideal material in the field of PDs, which has important value for imaging research.

Bi_2Te_3 PDs have been reported, including nanowires [16], nanobelts [17], heterojunction [18] and photoelectrochemical types [19]. Wang et al. prepared polycrystalline Bi_2Te_3 thin films using pulsed laser deposition at different growth temperatures, which exhibited excellent optoelectronic properties in the infrared band [20]. Zhang et al. used molecular beam epitaxy technology to directly grow high-quality Bi_2Te_3 topological insulator layers on GaAs chips and prepared heterojunction array PDs with a broadband light response [21]. However, nanowire and nanobelt PDs have shortcomings in response time, performance,

integration, commercialization, and manufacturing cost. The preparation process of heterojunction PDs is complex, costly, and requires consideration of energy level matching for different materials [22]. The photoelectric chemical type Bi_2Te_3 PD has low responsivity and service life [23]. Therefore, the research on Bi_2Te_3 thin film PDs has important potential and value.

In this paper, we have grown continuous and high-quality Bi_2Te_3 thin films on substrates using a dual-temperature-zone vapor deposition method. Under 405 nm illumination, the responsivity (R) of the device is 5.6 mA/W, the specific detectivity (D^*) is 1.22 $\times$ 10^7 Jones and the response time is 262/328 ms. The test results show that the Bi_2Te_3 thin-film material has excellent broadband spectral response and great potential for application in modern optoelectronic detection. In order to study the imaging performance of the device, we constructed a single-point scanning imaging system based on a Bi_2Te_3 PD and successfully obtained high-resolution imaging results for four digital images of "8358" at a wavelength of 532 nm.

2. Experimental

2.1. Material Synthesis and Device Preparation

Substrates were successively ultrasonically cleaned with acetone, isopropanol and deionized water. As shown in Figure S1, Bi_2Te_3 thin films were grown using a tube furnace through vapor deposition. Bi_2O_3 (99.995%, 0.1 g) powder was used as the Bi source, and Te (99.9999%, 1 g) granules were used as the Te source. Argon gas and hydrogen gas at flow rates of 200 sccm and 15 sccm, respectively were used as growth carrier gas. The growth equipment uses a dual-temperature-zone tube furnace, with Bi_2O_3 placed in the high-temperature zone and heated to 700 °C, and Te placed in the low-temperature zone and heated to 500 °C. The substrate was placed 7 cm below Bi_2O_3, at a temperature of about 450 °C, and grown for 15 min. Bi_2Te_3 thin films were grown on the substrate. Finally, 10 nm chromium and 300 nm gold were grown on the Bi_2Te_3 thin films by vacuum thermal evaporation to prepare Bi_2Te_3 PDs. The electrode structure is shown in Figure S2; it has a channel length of 0.05 mm and a channel width of 2.5 mm.

2.2. Material Characterization and Device Measurement

X-ray diffraction (XRD) (Bruker, Germany) was used to obtain X-ray diffraction patterns of the Bi_2Te_3 films. Field emission scanning electron microscopy (FE-SEM) (FEI, America) was used to characterize the surface of the Bi_2Te_3 films. Raman spectroscopy (Hrobia, Japan) was used to analyze internal molecular vibration patterns and intermolecular forces. The thickness and surface roughness images of the Bi_2Te_3 thin films were obtained using atomic force microscopy (AFM) (Bruker, Germany).

Two Au electrodes are connected to the two output ports of a Keithley 2400 as source and drain, and the channel current (I_{DS}) of the device was detected under the action of the applied drain-source voltage (V_{DS}). The photoelectric test is carried out under 405 nm, 532 nm and 808 nm illumination.

3. Results and Discussion

Bi_2Te_3 has a rhomboid structure belonging to the R-3m space group (a = b = 4.386 Å, c = 30.497 Å, and $\alpha = \beta = 90°$, $\gamma = 120°$) [24]. As shown in Figure 1a, the crystal structure of Bi_2Te_3 consists of five atomic layers Te-Bi-Te-Bi-Te [25,26], where the bonds within each quintuple layer are formed through strong covalent bonds, while the bonds between quintuple layers are formed through weak van der Waals forces [24]. This out-of-plane van der Waals interaction without surface dangling bonds helps to reduce the recombination noise generated by charge carriers [27,28]. The structure diagram of Bi_2Te_3 PD is shown in Figure 1b. The Bi_2Te_3 thin films are deposited on Si/SiO_2 substrates, and electrodes are evaporated onto the Bi_2Te_3 thin films. The surface SEM of the Bi_2Te_3 thin film shows a dense and uniform morphology as shown in Figure 1c, which gives the Bi_2Te_3 PD excellent optoelectronic performance. The energy band diagram is shown in Figure 1d. Due to the

high crystal quality of Bi_2Te_3, the localization effect of electrons is weak, exhibiting an enlarged excitable electron pool [20]. The carrier transport behavior can be explained by the carrier transport mechanism under illumination [29], such as carrier transitions, hot electron emissions and tunneling currents [30]. When the incident light is irradiated on the channel, the energy of the incident photon excites the transition of electrons from the valence band to the conduction band in Bi_2Te_3. Due to energy level differences, electrons and holes will transfer from Bi_2Te_3 to the electrodes on both sides, forming a photocurrent.

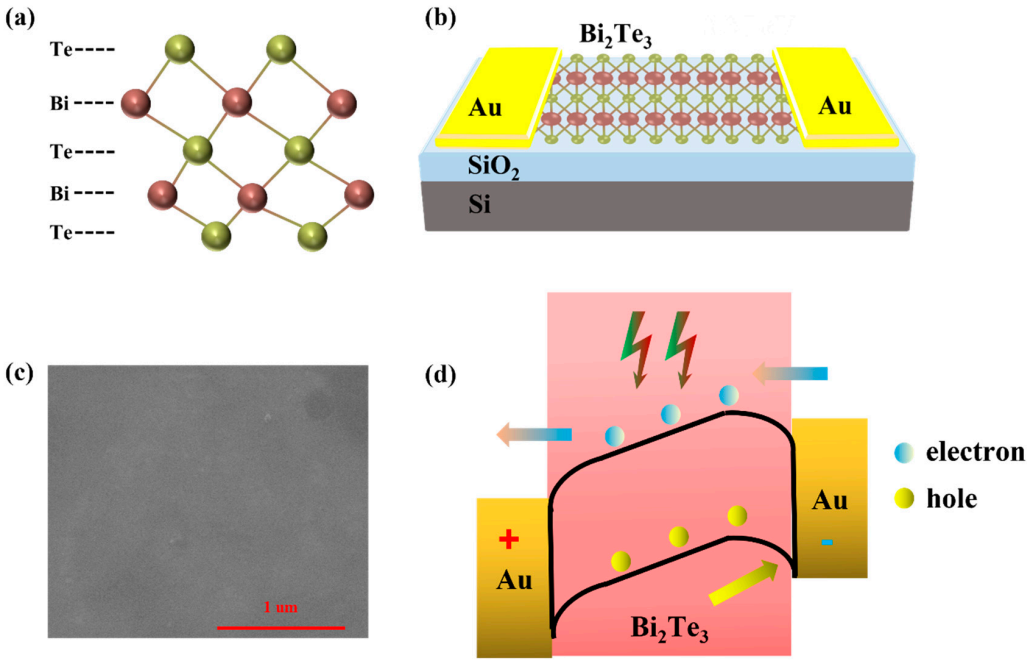

Figure 1. (**a**) Lattice structure of Bi_2Te_3. (**b**) Structure diagram of Bi_2Te_3 PD. (**c**) Surface SEM of Bi_2Te_3 thin film. (**d**) Energy band diagram of Bi_2Te_3 PD, arrows indicate the direction of electron and hole flow.

Figure 2a shows an AFM image of the Bi_2Te_3 thin film. The height distribution is shown in Figure 2b along the white dashed lines labeled in the AFM image, which shows that the thickness of the Bi_2Te_3 thin film used to fabricate the PD is about 12.31 nm. The Bi_2Te_3 thin film exhibits good surface roughness with a root mean square roughness of 1.11 nm. The Raman spectrum of Bi_2Te_3 is shown in Figure 2c, and two characteristic peaks can be observed, corresponding to the $E_g{}^2$ (123 cm^{-1}) and $A_{1g}{}^2$ (142 cm^{-1}) modes of the Bi_2Te_3 layer [31]. In order to further determine the crystal structure of the prepared Bi_2Te_3 and analyze the related properties, Bi_2Te_3 was characterized by XRD. The XRD diffraction pattern is shown in Figure 2d, with four diffraction peaks located at 2θ = 23.56°, 27.59°, 38.8°, and 40.5° corresponding to the (101), (015), (1.0.10), and (110) crystal planes of Bi_2Te_3 [32].

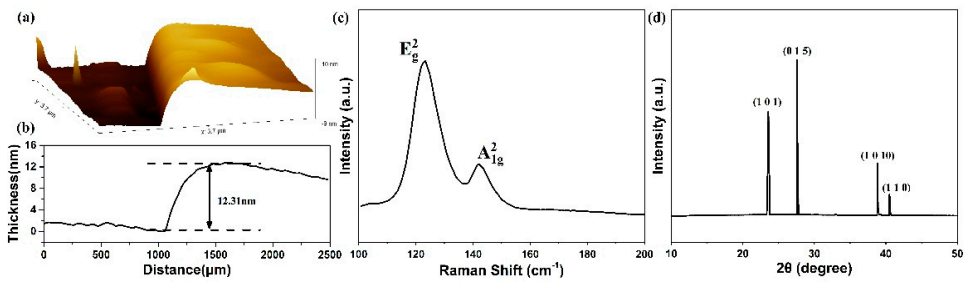

Figure 2. (**a**) AFM of Bi_2Te_3 thin film samples. (**b**) Thickness of Bi_2Te_3 thin film samples. (**c**) Raman spectrum of Bi_2Te_3 thin film samples. (**d**) X-ray diffraction pattern of Bi_2Te_3 thin film samples.

I-V curves of the Bi_2Te_3 PD are shown in Figure 3, Ohmic contact is formed between the Bi_2Te_3 thin film and Cr/Au metal electrodes [11]. The I_{DS} was modulated by V_{DS}, thus, the device worked as a photoconductive device. We studied the I_{DS} under different bias voltages and optical powers. Figure 3a–c show the I_{DS} of Bi_2Te_3 PDs at wavelengths of 405 nm, 532 nm and 808 nm at different incident powers. As can be seen, I_{DS} is highly dependent on bias voltage and incident light power. As the bias voltage increases, the I_{DS} shows an approximately linear increasing trend. Because bias is conducive to the separation and transport of photon-excited charge carriers, the integration amount of photogenerated charge carriers will significantly increase with an increase in the electric field [33]. It can be seen that at higher excitation intensities, more electron–hole pairs are generated, which is consistent with the observed fact that the I_{DS} increases monotonically with increasing excitation power [34].

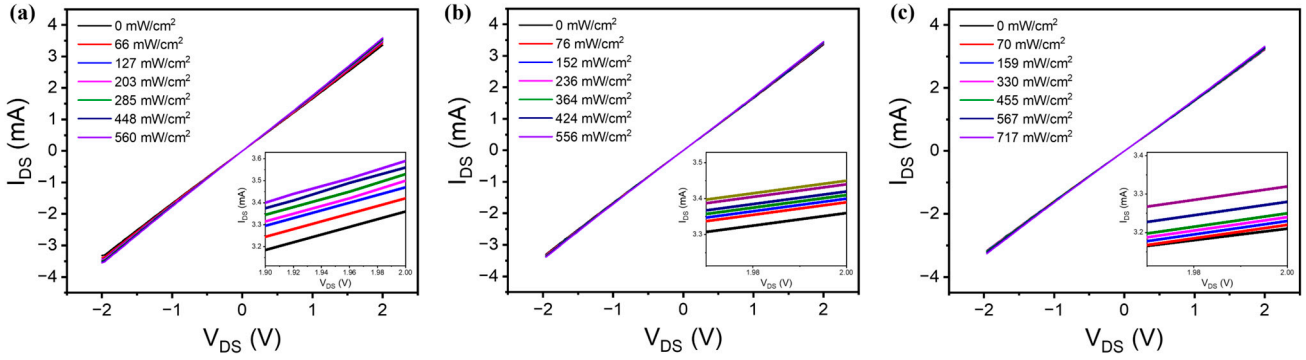

Figure 3. (**a**) I-V curves of Bi_2Te_3 PD under 405 nm illumination. (**b**) I-V curves of Bi_2Te_3 PD under 532 nm illumination. (**c**) I-V curves of Bi_2Te_3 PD under 808 nm illumination.

The light-response speed is another key factor that determines the ability of PD to track fast-switching light signals [35]. The time-dependent response curves of the Bi_2Te_3 PD at V_{DS} = 2 V are shown in Figure 4, the Bi_2Te_3 PD exhibited good periodic on-off switching. Optical response measurements were conducted under alternating on/off laser illumination. Figure 4a shows the photoelectric switching behavior under 405 nm laser irradiation at different excitation intensities and a 2 V bias voltage, indicating that the Bi_2Te_3 PD exhibits highly reversible and stable photoelectric switching behavior when laser irradiation alternates on/off [36]. In order to further understand the optical response of the Bi_2Te_3 PD, the performance of the device in air was measured under laser irradiation at 532 nm and 808 nm at a bias voltage of 2 V, as shown in Figure 4b,c. The I_{DS} gradually increases with an increase in light intensity, indicating that the photoconductive mechanism is the operating principle of the device [37]. The Bi_2Te_3 thin film has a unique topological insulator structure, and its carrier dynamics exhibit significant light-intensity dependence. The different electronic structures of surface and bulk electrons significantly affect the number of electrons excited by light [20]. The single period response is shown in Figure 4d,e, Under 405 nm, 532 nm and 808 nm illumination, the Bi_2Te_3 PD had the response speed of 328/338 ms, 262/328 ms and 365/277 ms, respectively.

R is defined as the ratio of the photocurrent or photovoltage of a PD to the incident light power [38]. D^* represents the signal-to-noise ratio generated by each unit of irradiation power of a PD at unit bandwidth and unit area, and is used to compare the detection capabilities of different PDs [39]. The R and D^* of the Bi_2Te_3 PD are shown in Figure 5. The R is calculated using the following equation [20]

$$R = \frac{\Delta I}{P} = \frac{I_{illu} - I_{dark}}{E_e \times A} \quad (1)$$

where I_{illu} represents the channel current under illumination, and I_{dark} represents the dark current. P, A and E_e are laser power, effective channel area and irradiance density, respectively. The D^* is calculated by the following equation [20]

$$D^* = R\sqrt{\frac{A}{2eI_{dark}}} \tag{2}$$

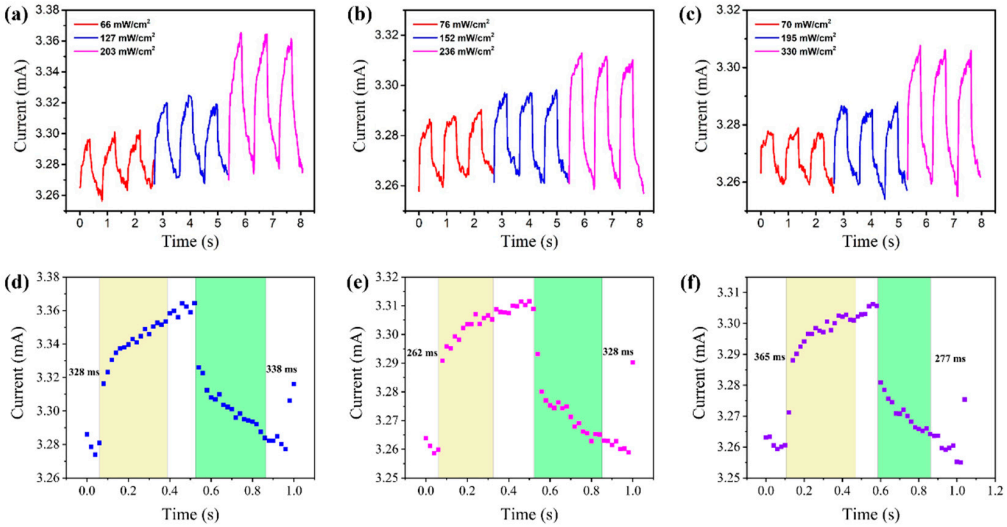

Figure 4. Time-dependent photoresponse of the Bi_2Te_3 PD under (**a**) 405 nm, (**b**) 532 nm and (**c**) 808 nm laser irradiation. Single-period response for rise and fall times under (**d**) 405 nm, (**e**) 532 nm and (**f**) 808 nm laser irradiation.

As shown in Figure 5, under 405 nm illumination (66 mW/cm^2), 532 nm illumination (78 mW/cm^2) and 808 nm illumination (70 mW/cm^2), the device has a maximum R of 5.6 mA/W, 5.3 mA/W and 4.8 mA/W, and a D^* of 1.22 × 10^7 Jones, 1.17 × 10^7 Jones and 1.13 × 10^7 Jones, respectively. The values of R and D^* decrease with the growing light intensity, which can be attributed to the increased recombination of photoexcited carriers under high light intensity [40]. External quantum efficiency (EQE) is another significant parameter for evaluating the performance of PD and is denoted by:

$$EQE = \frac{hcR_\lambda}{q\lambda} \tag{3}$$

where h is Plank's constant, c is the light velocity, q is the electronic charge, and λ is the incident light wavelength [41]. The EOE of the device under different optical power conditions is shown in Figure S3. It can be seen from the figure that the maximum EQE value is obtained at a wavelength of 405 nm, with a value of 1.7%.

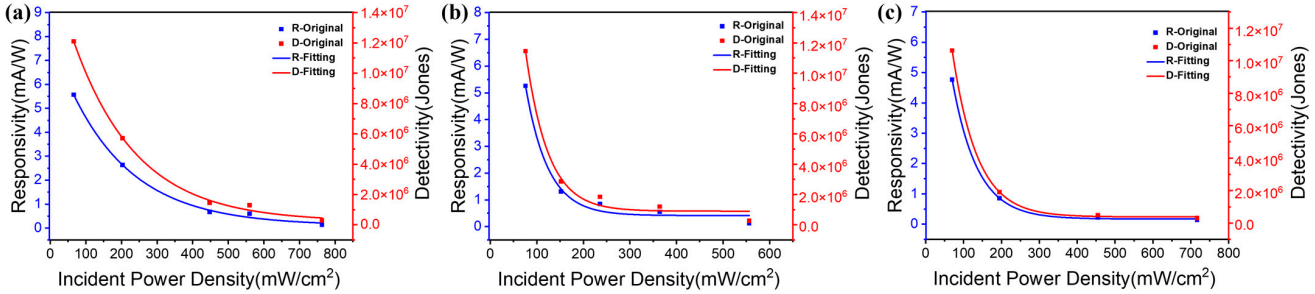

Figure 5. R and D^* of Bi_2Te_3 PD under (**a**) 405 nm, (**b**) 532 nm and (**c**) 808 nm laser irradiation at V_{DS} = 2 V.

In order to study the imaging performance of the device, we built a single-point scanning imaging system based on the Bi_2Te_3 PD, as shown in Figure 6a. The system includes a 532 nm laser, a 2D scanning platform, an image mask, and a Bi_2Te_3 PD. In the system, the laser fires a laser at a pre-designed image mask, such as our design of "8358" four digital images. By moving the mask, the laser can shine on different parts of the mask. With the movement of the mask, we can collect the change in the photocurrent signal of the device and record the photocurrent value at each position. Then, the changes in the optical signal are processed and calculated by an appropriate algorithm to generate a mapped image of the photocurrent. We successfully obtained the imaging results of four digital images of "8358" at a 532 nm wavelength, as shown in Figure 6b. From this result, we can speculate that similar effects can also be achieved at wavelengths of 405 nm and 808 nm. Based on these imaging results, the Bi_2Te_3 PD shows great potential at normal atmospheric pressure and room temperature and plays a role in promoting visible light imaging. This indicates that the Bi_2Te_3 device has good application prospects in imaging and is worthy of further research and exploration.

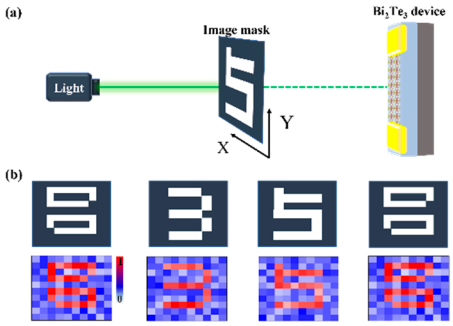

Figure 6. (**a**) Single-point scanning imaging system based on Bi_2Te_3 PD. (**b**) Imaging results of digital images at a 532 nm wavelength.

The performance of our Bi_2Te_3 PD and Bi_2Te_3 PDs in the literature were compared, as shown in Table 1. Compared with thin-film devices, the Bi_2Te_3 PD prepared by us has a faster response speed, with slightly lower R and D^*. Compared with nanosheets and nanoplate devices, our Bi_2Te_3 PD has relatively better performance. If we continue to study the process and device structure direction, we believe that we can obtain Bi_2Te_3 PDs with better performance. For example, improving the preparation process of Bi_2Te_3 to enhance film quality can accelerate device performance. In addition, the performance of the device can be improved by adding strategies, preparing dielectric layers, and constructing heterostructures.

Table 1. Performance comparison of Bi_2Te_3 PDs.

Materials	R (mA/W)	D^* (Jones)	Response Time (ms)	Ref
Bi_2Te_3 thin films	56.98	1.82×10^9	1.06/2.88	[20]
Bi_2Te_3 nanoplates	55.06	5.92×10^7	1.043/1.303	[11]
Bi_2Te_3 nanoplates	0.395	/	1/70	[42]
Bi_2Te_3 nanoplates	20.48	/	700/1480	[43]
Bi_2Te_3 nanoplates	4.91	7.73×10^9	14/99	[44]
Bi_2Te_3 thin films	5.6	1.22×10^7	262/328	This work

4. Conclusions

In summary, we prepared a Bi_2Te_3 PD by dual-temperature-zone vapor deposition, and the device exhibited excellent optoelectronic performance, which is attributed to the high-quality lattice structure and dense and uniform thin film. Under 405 nm illumination, the R of the prepared Bi_2Te_3 PD was 5.6 mA/W, D^* was 1.22×10^7 Jones, and the response time was 262/328 ms. We constructed a single-point scanning imaging system based on the prepared Bi_2Te_3 PD and successfully obtained high-resolution imaging results for four

digital images of "8358" at a wavelength of 532 nm. This work provides guidance for the application of 2D semiconductor materials, especially Bi_2Te_3, in the fields of photoelectric devices and imaging.

Supplementary Materials: The following supporting information can be downloaded at: https://www.mdpi.com/article/10.3390/photonics11111052/s1, Figure S1: Schematic diagram of the preparation process of Bi_2Te_3 thin-film samples; Figure S2: The electrode structure of the Bi_2Te_3 PD; Figure S3: The *EOE* of the device under different optical power conditions.

Author Contributions: Z.F., H.Z. and X.L. designed and conducted experiments. X.S. and F.W. participated in the analysis of data. W.S., L.D. and Y.S. designed the experimental scheme. Z.F. and X.L. wrote the manuscript. J.Y. revised the manuscript. All authors have read and agreed to the published version of the manuscript.

Funding: This research received no external funding.

Institutional Review Board Statement: Not applicable.

Informed Consent Statement: Not applicable.

Data Availability Statement: The data presented in this study are available on request from the corresponding author.

Acknowledgments: This research was supported by the National Key R&D Program of China (2019YFA0705204), the National Natural Science Foundation of China (62005107, 62005074), the Natural Science Foundation of Jiangsu Province (BK20180862, BK20190839) and the China Postdoctoral Science Foundation (2019M651725).

Conflicts of Interest: The authors declare that they have no known competing financial interests or personal relationships that could have appeared to influence the work reported in this paper.

References

1. Zhang, D.; Fuentes-Hernandez, C.; Vijayan, R.; Zhang, Y.; Li, Y.; Park, J.W.; Wang, Y.; Zhao, Y.; Arora, N.; Mirzazadeh, A.; et al. Flexible computational photodetectors for self-powered activity sensing. *npj Flex. Electron.* **2022**, *6*, 7. [CrossRef]
2. Cai, S.; Zuo, C.; Zhang, J.; Liu, H.; Fang, X. A Paper-Based Wearable Photodetector for Simultaneous UV Intensity and Dosage Measurement. *Adv. Funct. Mater.* **2021**, *31*, 2100026. [CrossRef]
3. Deng, M.; Li, Z.; Deng, X.; Hu, Y.; Fang, X. Wafer-scale heterogeneous integration of self-powered lead-free metal halide UV photodetectors with ultrahigh stability and homogeneity. *J. Mater. Sci. Technol.* **2023**, *164*, 150–159. [CrossRef]
4. Wang, P.; Xue, W.; Ci, W.; Yang, R.; Xu, X. Intrinsic vacancy in 2D defective semiconductor In_2S_3 for artificial photonic nociceptor. *Mater. Futures* **2023**, *2*, 035301. [CrossRef]
5. Ma, Y.; Deng, Z.; Liang, H.; Guan, X.; Zheng, Z.; Yao, J.; Yang, G. Wafer-Scale Fabrication of Broadband Sb_2Se_3 Photodetectors and their Multifunctional Optoelectronic Applications. *Laser Photonics Rev.* **2024**, *2024*, 2400669. [CrossRef]
6. Yan, T.; Li, Z.; Su, L.; Wu, L.; Fang, X. Bidirectional and Dual-Mode Organic Photodetector Enables Secure Ultraviolet Communication. *Adv. Funct. Mater.* **2023**, *33*, 2302746. [CrossRef]
7. Xing, R.; Li, Z.; Zhao, W.; Wang, D.; Xie, R.; Chen, Y.; Wu, L.; Fang, X. Waterproof and Flexible Perovskite Photodetector Enabled By P-type Organic Molecular Rubrene with High Moisture and Mechanical Stability. *Adv. Mater.* **2024**, *36*, 2310248. [CrossRef]
8. Zou, T.; Choi, T.; Liu, A.; Zhu, H.; Noh, Y.-Y. Printed quantum dot photodetectors for applications from the high-energy to the infrared region. *Nano Energy* **2024**, *125*, 109539. [CrossRef]
9. Zhao, C.; Wang, D.; He, W.; Liu, D.; Cao, J.; Zhang, X.; Liu, S.; Zhang, B.; Pan, J.; Zeng, Z.; et al. Photothermal synergistic high-sensitivity self-driven vertical asymmetric $Te/Bi_2Te_3/In_2O_3$ heterojunction near-infrared imaging photodetector. *Chem. Eng. J.* **2024**, *486*, 150183. [CrossRef]
10. Lu, C.; Luo, M.; Dong, W.; Ge, Y.; Han, T.; Liu, Y.; Xue, X.; Ma, N.; Huang, Y.; Zhou, Y.; et al. $Bi_2Te_3/Bi_2Se_3/Bi_2S_3$ Cascade Heterostructure for Fast-Response and High-Photoresponsivity Photodetector and High-Efficiency Water Splitting with a Small Bias Voltage. *Adv. Sci.* **2023**, *10*, 2205460. [CrossRef]
11. Liu, J.L.; Wang, H.; Li, X.; Chen, H.; Zhang, Z.K.; Pan, W.W.; Luo, G.Q.; Yuan, C.L.; Ren, Y.L.; Lei, W. Ultrasensitive flexible near-infrared photodetectors based on Van der Waals Bi_2Te_3 nanoplates. *Appl. Surf. Sci.* **2019**, *484*, 542–550. [CrossRef]
12. Pei, J.; Cai, B.; Zhuang, H.-L.; Li, J.-F. Bi_2Te_3-based applied thermoelectric materials: Research advances and new challenges. *Natl. Sci. Rev.* **2020**, *7*, 1856–1858. [CrossRef] [PubMed]
13. Ahmad, M.; Kodan, N.; Ghosh, A.; Mehta, B.R. The nature of 2D:3D SnS:Bi_2Te_3 interface and its effect on enhanced electrical and thermoelectric properties. *J. Alloys Compd.* **2020**, *847*, 156233. [CrossRef]
14. Tang, X.; Li, Z.; Liu, W.; Zhang, Q.; Uher, C. A comprehensive review on Bi_2Te_3-based thin films: Thermoelectrics and beyond. *Interdiscip. Mater.* **2022**, *1*, 88–115. [CrossRef]

15. Culcer, D.; Cem Keser, A.; Li, Y.; Tkachov, G. Transport in two-dimensional topological materials: Recent developments in experiment and theory. *2d Mater.* **2020**, *7*, 022007. [CrossRef]
16. Jeong, K.; Park, D.; Maeng, I.; Kim, D.; Kwon, H.; Kang, C.; Cho, M.-H. Modulation of optoelectronic properties of the Bi_2Te_3 nanowire by controlling the formation of selective surface oxidation. *Appl. Surf. Sci.* **2021**, *548*, 149069. [CrossRef]
17. Zhao, T.; Zhong, F.; Wang, S.; Wang, Y.; Xu, T.; Chen, Y.; Yu, Y.; Guo, J.; Wang, Z.; Yu, J.; et al. Hydrogen-Assisted Synthesis of Large-Size 2D Bismuth Telluride Flakes for Broadband Photodetection up to 2 μm. *Adv. Opt. Mater.* **2023**, *11*, 2202208. [CrossRef]
18. Zhao, C.; Wang, D.; Cao, J.; Zeng, Z.; Zhang, B.; Pan, J.; Liu, D.; Liu, S.; Jiao, S.; Chen, T.; et al. Highly efficient 1D p-Te/2D n-Bi_2Te_3 heterojunction self-driven broadband photodetector. *Nano Res.* **2024**, *17*, 1864–1874. [CrossRef]
19. Ren, X.; Zheng, W.; Qiao, H.; Ren, L.; Liu, S.; Huang, Z.; Qi, X.; Wang, Z.; Zhong, J.; Zhang, H. Enhanced photoresponse behavior of Au@Bi_2Te_3 based photoelectrochemical-type photodetector at solid-solid-liquid joint interface. *Mater. Today Energy* **2020**, *16*, 100401. [CrossRef]
20. Kao, Q.; Xiao, Y.; Jia, Y.; Wang, J.; Wang, C. Infrared photoelectric detection of polycrystalline Bi_2Te_3 thin films prepared by pulsed laser deposition. *J. Vac. Sci. Technol. A* **2024**, *42*, 023421. [CrossRef]
21. Zhang, X.; Liu, X.; Zhang, C.; Peng, S.; Zhou, H.; He, L.; Gou, J.; Wang, X.; Wang, J. Epitaxial Topological Insulator Bi_2Te_3 for Fast Visible to Mid-Infrared Heterojunction Photodetector by Graphene As Charge Collection Medium. *ACS Nano* **2022**, *16*, 4851–4860. [CrossRef] [PubMed]
22. Huo, N.; Konstantatos, G. Recent Progress and Future Prospects of 2D-Based Photodetectors. *Adv. Mater.* **2018**, *30*, 1801164. [CrossRef] [PubMed]
23. Sreedhar, A.; Noh, J.-S. Realization of electrolyte interface effect on Bi_2Te_3 implanted flake-like ZnO thin films for understanding the highly stable PEC water splitting under simulated solar light and visible light. *Mater. Res. Express* **2021**, *8*, 016405. [CrossRef]
24. Yu, L.; Tian, P.; Tang, L.; Zuo, W.; Zhong, H.; Hao, Q.; Teng, K.S.; Zhao, G.; Su, R.; Gong, X.; et al. Room Temperature Broadband Bi_2Te_3/PbS Colloidal Quantum Dots Infrared Photodetectors. *Sensors* **2023**, *23*, 4328. [CrossRef] [PubMed]
25. Wang, G.; Meng, F.; Chen, Y.; Lotnyk, A.; Shen, X. Boosting Thermoelectric Performance of Bi_2Te_3 Material by Microstructure Engineering. *Adv. Sci.* **2024**, *11*, 2308056. [CrossRef]
26. Teweldebrhan, D.; Goyal, V.; Rahman, M.; Balandin, A.A. Atomically-thin crystalline films and ribbons of bismuth telluride. *Appl. Phys. Lett.* **2010**, *96*, 053107. [CrossRef]
27. Liang, S.-J.; Cheng, B.; Cui, X.; Miao, F. Van der Waals Heterostructures for High-Performance Device Applications: Challenges and Opportunities. *Adv. Mater.* **2020**, *32*, 1903800. [CrossRef]
28. Wang, F.; Zhang, T.; Xie, R.; Liu, A.; Dai, F.; Chen, Y.; Xu, T.; Wang, H.; Wang, Z.; Liao, L.; et al. Next-Generation Photodetectors beyond Van Der Waals Junctions. *Adv. Mater.* **2024**, *36*, 2301197. [CrossRef]
29. Dang, V.Q.; Han, G.-S.; Trung, T.Q.; Duy, L.T.; Jin, Y.-U.; Hwang, B.-U.; Jung, H.-S.; Lee, N.-E. Methylammonium lead iodide perovskite-graphene hybrid channels in flexible broadband phototransistors. *Carbon* **2016**, *105*, 353–361. [CrossRef]
30. Bansal, P.; Zhang, X.; Wang, H.; Kar, P.; Yu, W.W. Charge transfer between lead halide perovskite nanocrystals and single-walled carbon nanotubes. *Nanoscale Adv.* **2020**, *2*, 808–813. [CrossRef]
31. He, R.; Sucharitakul, S.; Ye, Z.; Keiser, C.; Kidd, T.E.; Gao, X.P.A. Laser induced oxidation and optical properties of stoichiometric and non-stoichiometric Bi_2Te_3 nanoplates. *Nano Res.* **2015**, *8*, 851–859. [CrossRef]
32. Hu, L.; Liu, C.; Zhang, F.; Wang, H.; Wang, B. Vacancy-Defect Ternary Topological Insulators Bi_2Se_2Te Encapsulated in Mesoporous Carbon Spheres for High Performance Sodium Ion Batteries and Hybrid Capacitors. *Small* **2024**, *20*, 2311079. [CrossRef] [PubMed]
33. Ouyang, W.; Teng, F.; He, J.-H.; Fang, X. Enhancing the Photoelectric Performance of Photodetectors Based on Metal Oxide Semiconductors by Charge-Carrier Engineering. *Adv. Funct. Mater.* **2019**, *29*, 1807672. [CrossRef]
34. Liu, J.; Li, Y.; Song, Y.; Ma, Y.; Chen, Q.; Zhu, Z.; Lu, P.; Wang, S. Bi_2Te_3 photoconductive detectors on Si. *Appl. Phys. Lett.* **2017**, *110*, 141109. [CrossRef]
35. Yu, Y.; Zhang, Y.; Zhang, Z.; Zhang, H.; Song, X.; Cao, M.; Che, Y.; Dai, H.; Yang, J.; Wang, J.; et al. Broadband Phototransistor Based on $CH_3NH_3PbI_3$ Perovskite and PbSe Quantum Dot Heterojunction. *J. Phys. Chem. Lett.* **2017**, *8*, 445–451. [CrossRef]
36. Liu, J.L.; Chen, H.; Li, X.; Wang, H.; Zhang, Z.K.; Pan, W.W.; Yuan, G.; Yuan, C.L.; Ren, Y.L.; Lei, W. Ultra-fast and high flexibility near-infrared photodetectors based on Bi_2Se_3 nanobelts grown via catalyst-free van der Waals epitaxy. *J. Alloys Compd.* **2020**, *818*, 152819. [CrossRef]
37. Cao, R.; Wang, H.-D.; Guo, Z.-N.; Sang, D.K.; Zhang, L.-Y.; Xiao, Q.-L.; Zhang, Y.-P.; Fan, D.-Y.; Li, J.-Q.; Zhang, H. Black Phosphorous/Indium Selenide Photoconductive Detector for Visible and Near-Infrared Light with High Sensitivity. *Adv. Opt. Mater.* **2019**, *7*, 1900020. [CrossRef]
38. Wang, F.; Zhang, T.; Xie, R.; Wang, Z.; Hu, W. How to characterize figures of merit of two-dimensional photodetectors. *Nat. Commun.* **2023**, *14*, 2224. [CrossRef]
39. Yang, D.; Ma, D. Development of Organic Semiconductor Photodetectors: From Mechanism to Applications. *Adv. Opt. Mater.* **2019**, *7*, 1800522. [CrossRef]
40. Roy, K.; Padmanabhan, M.; Goswami, S.; Sai, T.P.; Ramalingam, G.; Raghavan, S.; Ghosh, A. Graphene–MoS_2 hybrid structures for multifunctional photoresponsive memory devices. *Nat. Nanotechnol.* **2013**, *8*, 826–830. [CrossRef]
41. Liu, X.; Wang, D.; Shao, P.; Sun, H.; Fang, S.; Kang, Y.; Liang, K.; Jia, H.; Luo, Y.; Xue, J.; et al. Achieving Record High External Quantum Efficiency >86.7% in Solar-Blind Photoelectrochemical Photodetection. *Adv. Funct. Mater.* **2022**, *32*, 2201604. [CrossRef]

42. Zhang, Y.; You, Q.; Huang, W.; Hu, L.; Ju, J.; Ge, Y.; Zhang, H. Few-layer hexagonal bismuth telluride (Bi_2Te_3) nanoplates with high-performance UV-Vis photodetection. *Nanoscale Adv.* **2020**, *2*, 1333–1339. [CrossRef] [PubMed]
43. Zang, C.; Qi, X.; Ren, L.; Hao, G.; Liu, Y.; Li, J.; Zhong, J.J. Photoresponse properties of ultrathin Bi2Se3 nanosheets synthesized by hydrothermal intercalation and exfoliation route. *Appl. Surf. Sci.* **2014**, *316*, 341–347. [CrossRef]
44. Yang, S.; Jiao, S.; Nie, Y.; Zhao, Y.; Gao, S.; Wang, D.; Wang, J.; Li, Y. Boosting photoresponse and stability of a self-powered photoelectrochemical-type Bi_2Te_3 imaging photodetector by a novel quasi-solid-state gel electrolyte. *J. Alloys Compd.* **2024**, *982*, 173718. [CrossRef]